Research Square

Preprints are preliminary reports that have not undergone peer review.
They should not be considered conclusive, used to inform clinical practice,
or referenced by the media as validated information.

Hydrodynamic Impact of Cavitating Jets on Marine-Coated Steel Surfaces: Parametric Analysis and Non-Destructive Cleaning Performance

Ahmed MOUHLI

ahmedmouhli46@gmail.com

Science and Technology for Defense Laboratory, Military Research Center, Tunisia

Saber Hachicha

Research Laboratory of Marine Technology & Naval Systems, Naval Academy, Tunisia

Arwa Toumi

Laboratory of Energy and Environment, National Engineering School of Tunis (ENIT), Tunisia

Chadha Mejri

Research Laboratory of Marine Technology & Naval Systems, Naval Academy, Tunisia

Chiheb Zaoui

Research Laboratory of Marine Technology & Naval Systems, Naval Academy, Tunisia

Ahmed Siala

Science and Technology for Defense Laboratory, Military Research Center, Tunisia

Article

Keywords: biofouling removal, cavitating water jet, CFD simulation, low-cost nozzle design, non-destructive cleaning, stand-off distance

Posted Date: November 12th, 2026

DOI: https://doi.org/10.21203/rs.3.rs-11278659/v1

License: This work is licensed under a Creative Commons Attribution 4.0 International License.
Read Full License

Additional Declarations: No competing interests reported.

Hydrodynamic Impact of Cavitating Jets on Marine-Coated Steel Surfaces: Parametric Analysis and Non-Destructive Cleaning Performance

Ahmed Mouhli [1,*], Saber Hachicha [1], Arwa Toumi [3], Chadha Mejri [2], Chiheb Zaoui [2], Ahmed Siala [1]

[1] Science and Technology for Defense Laboratory, Military Research Center, Tunisia

[2] Laboratory LR-19-DN02, Tunisian Naval Academy, Menzel Bourguiba, Tunisia

[3] Laboratory of Energy and Environment, National Engineering School of Tunis (ENIT), Tunisia

Corresponding author: Ahmed Mouhli (ahmedmouhli46@gmail.com)

Abstract

Biofouling on ship hulls increases hydrodynamic drag, fuel consumption, and lifecycle maintenance costs. This work presents a quantitative experimental investigation of normal impact forces generated by cavitating and conventional high-pressure water jets on marine-coated carbon-steel surfaces. Analytical calculations and computational fluid dynamics (CFD) simulations were performed to evaluate internal flow and cavitation dynamics. Normal forces were measured using a calibrated load cell as a function of stand-off distance ([0,01-0,35] m) and jet incidence angle ([0,349–1,57] rad) under submerged conditions. The cavitating jet was generated by an in-house developed Venturi-type stainless-steel nozzle costing under €40. Results show that the cavitating jet delivered a quasi-stable normal force of 4.5 ± 0.2 N over [0,01–0,04] m, decaying by only 22% at 0,35 m (3.5 N), whereas the conventional jet force decayed rapidly. Surface characterization combining profilometry and dry-film-thickness monitoring confirmed a cleaning efficiency of 72

± 6% at the optimal window (d = [0,02–0,04] m, θ = [0,524– 0.786] rad) with no measurable coating degradation. These results demonstrate the suitability of low-cost cavitating jets for coating-safe underwater maintenance and provide operational guidelines directly applicable to autonomous marine cleaning systems.

Keywords: biofouling removal, cavitating water jet, CFD simulation, low-cost nozzle design, non-destructive cleaning, stand-off distance**.**

1. Introduction

Marine biofouling — the accumulation of biological organisms on submerged hull surfaces — is one of the most persistent operational, economic, and environmental challenges in the maritime sector. Laboratory-scale drag measurements indicate powering penalties as high as 86% at cruising speed for heavy calcareous fouling [1], while a light film covering only half of the hull can raise fuel consumption by up to 40% [2], on average, biofouling increases skin-friction drag by about 40% [3]. At the fleet scale, hull fouling for a single class of naval destroyers has been estimated at USD 56 million per year — roughly USD 1 billion over 15 years — with fuel overconsumption dominating the bill [4]. Beyond direct costs, fouling raises greenhouse-gas emissions and conflicts with IMO decarbonization targets [5]: a slime layer as thin as 0.0005 m over half the hull can increase emissions by 20-25% depending on ship type and speed [6]. Together, these findings make efficient, low-cost, coating-safe hull maintenance a lever for both operational performance and environmental compliance.

High-pressure water jetting (HPWJ) is the most widely adopted technique for in-situ removal of biofouling from coated steel, owing to its flexibility, absence of chemicals, and high removal efficiency [7-8]. At pressures typically between 2.10^7 and 6.10^7 Pascal, HPWJ can clean without

damaging antifoul coatings when jet angle, stand-off distance, and impingement duration are tightly controlled [9-10], maintaining such precision underwater, however, is rarely achievable in practice. Under alternating jet loading, fatigue and cavitation failure can appear on the substrate — spalling pits, layer erosion, and cavitation-hole morphology — with measurable effects on the brittleness and tensile strength of the steel [11]. Surface roughness varies non-monotonically with jet pressure, first rising and then falling, which complicates the definition of a universally safe operating window [12]. Moreover, the forces required for effective fouling removal, and their effect on coatings, remain incompletely quantified [13-14]. Environmentally, in-water cleaning can release antifouling-paint particles and biocides, with copper and zinc emissions far exceeding common water-quality standards [15], reactive cleaning of heavy fouling requires aggressive machinery that damages coatings and discharges paint and biofouling debris [16-17]. These cumulative limitations motivate cleaning approaches that combine effective removal with guaranteed coating preservation.

Cavitating water jets have emerged as a non-destructive alternative. Their mechanism relies on the controlled collapse of vapor cavities generated under hydrodynamic cavitation, producing highly localized micro-jets and shock waves at the surface [18-19-20]. The impact pressure of a cavitating jet can exceed that of a continuous jet of equal flow rate by one to two orders of magnitude, enabling targeted fouling detachment at much lower macroscopic loading; the impact load is governed primarily by stand-off distance, with nozzle-outlet geometry also strongly influential, as established by high-speed imaging combined with grayscale analysis [21]. Submerged cavitating jets have been shown to remove marine organisms from hulls without damaging the paint, with stable erosion at 0,03-0,05 m stand-off for optimized shear-nozzle geometries [22], and robotic

66 platforms integrating cavitation modules have been field-demonstrated while limiting hull damage
67 and debris dispersal [23].

68 Despite this progress, quantitative characterization of cavitating-jet / coated-surface interaction
69 remains incomplete. First, most studies use erosion patterns and mass loss as performance metrics
70 [24], whereas direct measurement of the normal impact force versus operating parameters is
71 largely absent from the literature in a coating-preservation context; an absolute force scale is still
72 lacking for translating cavitation cleaning into design-relevant cleaning forces. Second, although
73 stand-off distance is known to control erosion intensity, no study has systematically mapped
74 normal-force evolution across the full operational range ([0,01-0,35] m) relevant to robotic
75 deployment. Third, the combined effect of stand-off distance and incidence angle on force stability
76 — critical for cleaning geometrically complex hulls — has not been quantified under
77 representative submerged conditions.

78 This study addresses these gaps through three original contributions: (i) systematic quantification
79 of the normal impact forces of both cavitating and conventional high-pressure jets on multilayer
80 marine-coated carbon steel, across d = [0,01-0,35] m and θ = [0,349 - 1,57] rad, providing the first
81 comprehensive submerged force map for this parameter space; (ii) parametric identification of the
82 optimal operating window enabling effective fouling removal while preserving coating integrity,
83 directly applicable to autonomous cleaning-robot design; and (iii) design, fabrication, and
84 validation of a low-cost Venturi cavitating nozzle (material cost < €40, a > 99% reduction versus
85 ~€5000 commercial equivalents), demonstrating that high-performance cavitating cleaning is
86 achievable with accessible, replicable hardware.

87 **2. Materials and Methods**

88 **2.1. Biofouling formation and sample preparation**

2.1.1. Substrate and coating system

Test specimens were carbon-steel plates (grade S235JR, 0,3 × 0,2 × 0,006 m) representative of hull structural steel. Prior to coating, all surfaces were abrasive-blasted to cleanliness grade Sa 2.5 (ISO 8501-1) [25], removing mill scale, rust, and contaminants to a near-white finish; the surface profile, measured with a Mitutoyo TR-200 profilometer, was maintained at 50-75 µm Rz to ensure adhesion. A three-layer marine protective system was applied under controlled workshop conditions (20 ± 2 °C (293,15 ± 2 K), RH < 75%): a two-component epoxy anticorrosion primer (DFT = 80 ± 5 µm (80 ± 5.10^{-6} m)), a polyurethane intermediate coat (DFT = 60 ± 5 µm (60 ± 5 .10^{-6} m)), and a hard-matrix antifouling topcoat (DFT = 75 ± 5 µm (75 ± 5 .10^{-6} m)), for a nominal total of 215 µm (215. 10^{-6} m). Thickness was verified after each coat at five points per plate with a calibrated magnetic-induction gauge (Elcometer 456 ±1 µm (456 ±1 .10^{-6} m); ISO 19840) [26], and a minimum 7-day cure preceded immersion. Thirty specimens were prepared identically: 12 for cavitating-jet tests, 12 for conventional-jet tests, and 6 as unprocessed references; inter-sample thickness variability was below ±8 µm (8.10^{-6} m) (< 4% of total DFT).

2.1.2. Controlled biofouling formation

Natural biofouling was induced by immersing the coated plates in a static seawater tank (volume ≈ 250 L (0,25 m^3)) under laboratory conditions approximating a coastal environment: 20 ± 2 °C (293,15 ± 2 K), salinity = 35 ± 2 PSU, *pH* = 8 ± 0.2, and dissolved oxygen 0,006-0,008 kg/m³, monitored daily with a calibrated multiparameter probe. No forced flow was applied, consistent with quiescent harbour conditions [27-28]. Specimens were submerged 0,30 ± 0,01 m below the surface, corresponding to a hydrostatic back-pressure P_{hydro} = ρgh ≈ 2943 Pascal — negligible relative to the 1,2.10^7 Pascal operating pressure but retained in the cavitation-number calculation.

Plates were inspected weekly for three weeks and biweekly thereafter over a 70-day period (Figure 1).

By day 70, specimens showed a mature, heterogeneous fouling layer: a basal microbial biofilm, filamentous green algae (Ulva sp. and Cladophora sp.), and scattered sessile macrofoulers including barnacle cyprids (Amphibalanus sp., 800-1500 individuals per m^2). Pre-test characterization yielded mean roughness Ra = 28.4 ± 3.1 µm (versus 1.2 ± 0.2 µm (1.2 ± 0.2 $.10^{-6}$ m) on the clean reference; ISO 4287) [29], fouling coverage C_{fouled} = 91 ± 4% (ImageJ, n = 6), and an NSTM Chapter-633 fouling rating of 65-75 (heavy slime and algal coverage), confirming a consistent, severe fouling state across all specimens [30].

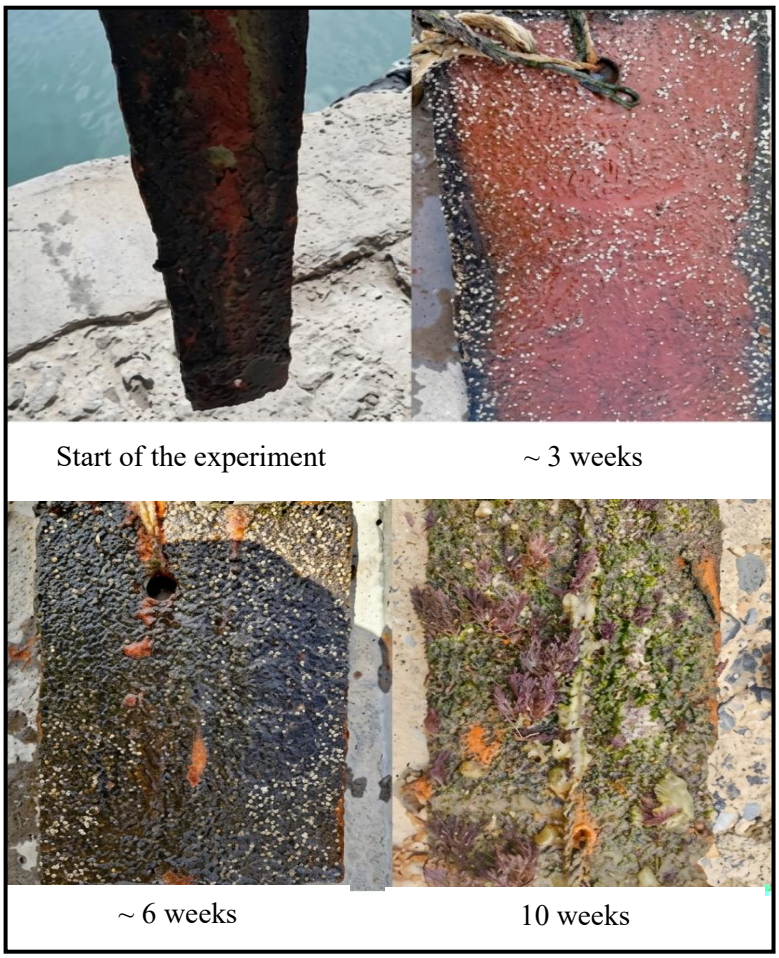


Figure 1. Progressive development of micro- and macrofouling on a coated steel plate over 70 days of immersion in static seawater (approximately 3, 6, and 10 weeks).

2.2. Theoretical framework: jet impact-force analysis

The hydrodynamic force of a water jet impinging on a flat surface depends on the jet momentum and on the geometry relative to the target. L et θ be the impingement angle measured between the jet axis and the target surface, so that $\theta = 1{,}57$ rad is perpendicular impingement and $\theta \rightarrow 0$ rad is grazing incidence. The total force F decomposes into a normal component F_n and a tangential component F_t (Figure 2):

$$F_n = F \sin \theta,\ F_t = F \cos \theta \quad (1)$$

This convention is applied throughout. In biofouling removal, F_n governs interfacial fatigue and decohesion at the fouling-coating interface, while F_t drives shear-induced detachment and lateral transport of dislodged particles.

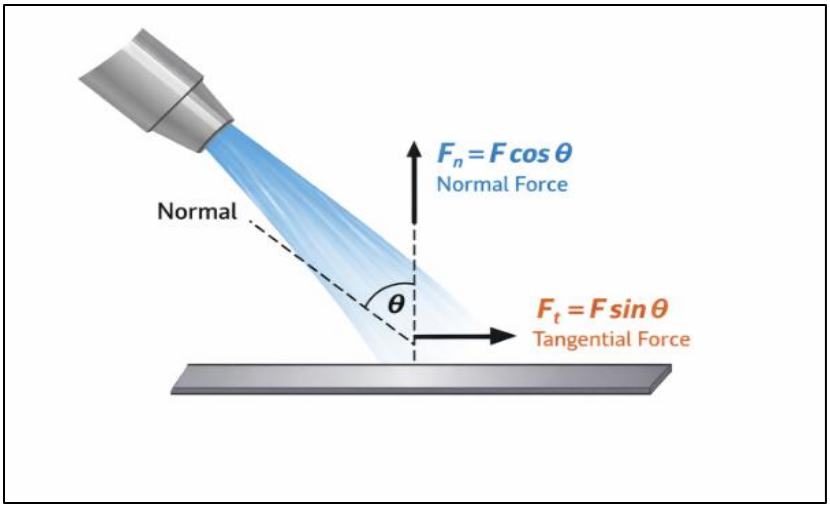


Figure 2. Decomposition of a water jet impinging on a plate into its normal (F_n) and tangential (F_t) components at incidence angle θ (measured from the target surface).

2.2.1. Conventional (non-cavitating) jet

For a steady, incompressible jet impinging normally on a rigid surface, conservation of linear momentum gives the total force [31]:

$$F = \dot{m}V = \rho QV = \rho AV^2 \quad (2)$$

where ρ is water density, Q the volumetric flow rate, A the jet cross-sectional area, and V the mean jet velocity. Projected onto the surface directions, $F_n = \rho AV^2 \sin\theta$ and $F_t = \rho AV^2 \cos\theta$. The effectiveness of conventional jets degrades rapidly with stand-off distance because of viscous dissipation and jet spreading.

2.2.2. Cavitating jet

In a cavitating jet, the total impact force combines the mean hydrodynamic jet force, the impulsive force from cavity collapse, and a pulsating force from repeated shock-wave emissions [18-32]:

$$F_{cav} = F_{jet} + F_{collapse} + F_{puls} \quad (3)$$

The mean jet force follows the momentum formulation, $F_{jet} = \rho AV^2$. The collapse force arises from impulsive pressures generated when a cavity collapses near the surface, producing micro-jets with velocities of 100-500 m/s, it is modelled as a fraction of the mean jet force through a dimensionless cavitation-intensity coefficient C_c:

$$F_{collapse} = C_c\, \rho AV^2 \quad (4)$$

The pulsating component reflects periodic shock-wave emissions from bubble collapse in the jet core. From spectral analysis of the raw force signal at the reference condition (θ = 1,57 rad, d = 0,02 m), the RMS force fluctuation was ΔF_{rms} = 0.18 ± 0.04 N, corresponding to $V_{rms} \approx$ 9.5 m/s

(about 16% of the throat velocity), consistent with pulsating-cavitation regimes reported for similar Venturi geometries [33-16]:

$$F_{puls} = \rho A \, V_{rms}^2 \quad (5)$$

Combining the three contributions and projecting onto the surface directions:

$$F_{n,cav} = \rho A[V^2(1 + C_c) + V_{rms}^2] \sin\theta \quad (6)$$

$$F_{t,cav} = \rho A[V^2(1 + C_c) + V_{rms}^2] \cos\theta \quad (7)$$

For $C_c = 0$ and $V_{rms} = 0$ these reduce to the conventional-jet expressions, ensuring physical consistency. The relevant velocity for the impinging momentum is the divergent-exit velocity $V \approx$ 29 m/s (from continuity at the exit diameter, Section 2.3), which gives a mean jet force $\rho A V^2 \approx$ 3.40 N, the higher throat velocity $V_{th} = 58$ m/s governs cavitation inception only. The coefficient C_c was calibrated from the measured normal force at the reference condition, $F_{n,meas} = 4.50 \pm 0.14$ N, with $F_{puls} = 0.18$ N, $C_c = (F_{n,meas} - \rho A V^2 - F_{puls})/(\rho A V^2) = (4.50 - 3.40 - 0.18)/3.40 = 0.27 \pm 0.04$. This value lies within the 0.15-0.30 range reported by Li & Soyama [33] for Venturi nozzles, providing independent confirmation of its plausibility. Equations (6)-(7), with $C_c = 0.27$ and $V_{rms} = 9.5$ m/s, are used for the theory-experiment comparison in Section 3.

2.3. Cavitating-nozzle design

The nozzle employs a convergent-divergent Venturi geometry designed to generate stable hydrodynamic cavitation under submerged conditions, following established principles for Venturi cavitation reactors in which a throat pressure drop, followed by controlled recovery in the divergent section, drives cavity nucleation, growth, and collapse [32-34].

2.3.1. Geometry and parameter selection

Key geometric parameters (Table 1) were selected from optimization guidelines for hydrodynamic-cavitation reactors [35-36]. The 0,786 rad convergent angle enhances cavitation intensity relative to shallower angles, the 0,14 rad divergent angle lies within the recommended [0,105 - 0,14] rad range promoting progressive pressure recovery; the throat length was set to twice the throat diameter to favour stable, resonant cavitation; and the contraction ratio $\beta = 0.20$ provides the velocity amplification needed for inception at $1{,}2.10^7$ Pascal. The divergent section expands the throat (0,0016 m) to an exit diameter of ≈ 0,00226 m, so the exit velocity (≈ 29 m/s) governs the impinging momentum while the throat velocity (58 m/s) governs cavitation.

Table 1. Geometric and hydraulic parameters of the designed cavitating nozzle.

Parameter	Symbol	Value	Unit
Inlet diameter	D_{in}	0,008	m
Throat diameter	d_{th}	0,0016	m
Exit diameter (divergent)	d_{ex}	≈ 0,00226	m
Contraction ratio	$\beta = d_{th} / D_{in}$	0.20	-
Convergent angle	α_c	0,786	rad
Divergent angle	α_d	0,14	rad
Throat length	L_{th}	0,0032 (= 2 d_{th})	m
Total length	L	0,05	m
Operating pressure	P	$1{,}2.10^7$	Pascal
Nominal flow rate	Q	$1{,}17 \times 10^{-4}$	m^3/s
Material	-	AISI 316L stainless steel	-

2.3.1. Geometry and parameter selection

Cavitation onset is characterized by the dimensionless cavitation number σ [37]:

$$\sigma = (P_{out} - P_v) / (\tfrac{1}{2} \rho V_{th}^2) \quad (8)$$

where P_{out} is the outlet (back) pressure, P_v the vapour pressure (≈ 2340 Pa at 20°C (293,15 K)), ρ = 1000 kg/m³, and V_{th} the throat velocity. Inception occurs for $\sigma \leq \sigma_i$. The derived operating quantities are summarized in Table 2.

Table 2. Calculated operating parameters confirming developed cavitation. The mean jet (impact) force is evaluated at the divergent exit; the throat-based value (6.8 N) is an upper bound not reached at the plate.

Parameter	Symbol	Value	Unit
Volumetric flow rate	Q	1.17×10^{-4}	m³/s
Throat cross-section	A_{th}	2.01×10^{-6}	m²
Throat velocity	V_{th}	≈ 58	m/s
Exit velocity	V_{ex}	≈ 29	m/s
Mass flow rate	$\dot{m} = \rho Q$	0.117	kg/s
Upstream pressure	P_1	12×10^6	Pa
Outlet pressure (0.3 m depth)	P_{out}	$\approx 1.03 \times 10^5$	Pa
Vapour pressure (20 °C)	P_v	2340	Pa
Cavitation number	σ	≈ 0.060	-
Mean jet impact force	$F_{jet} = \rho Q V_{ex}$	≈ 3.4	N

The cavitation number $\sigma \approx 0.060$ is well below the typical inception threshold for Venturi nozzles ($\sigma_i \approx 0.3$-1.5) [32-37], confirming operation in the developed-cavitation regime and consistent with the cavitation structures observed during testing (Section 3.4).

2.3.3. Numerical Simulation of Cavitating Flow Within the Nozzle

2.3.3.1. Governing Equations and Cavitation Modeling

- **Multiphase Flow Model**

The complex flow field under investigation is characterized by a gas–liquid multiphase flow. In numerical simulations, such flows can be resolved using either Euler-Euler or Euler-Lagrange approaches depending on the physical assumptions. While the Eulerian-Lagrangian framework tracks individual discrete trajectories, it demands significant computational resources. Therefore, to optimize computational efficiency while capturing the macro-hydrodynamics of the system, a Eulerian multiphase approach is preferred when individual discrete phase behaviors are not the primary focus. In this study, the Mixture model was employed to simulate the multiphase flow field. This model solves the continuity and momentum equations for the mixture, alongside volume fraction equations for the secondary phases, treating the phases as interpenetrating continua. The governing equations of the Mixture model are formulated as follows [22]:

The mixture continuity equation is formulated as follows:

$$\frac{\partial}{\partial t}(\rho_m) + \nabla \cdot (\rho_m \vec{v}_m) = 0 \tag{9}$$

Where $\overrightarrow{v_m}$ represents the mass-weighted average Velocity:

$$\vec{v}_m = \sum_{k=1}^{n} \alpha_k \rho_k \vec{v}_k / \rho_m \tag{10}$$

And ρ_m denotes the mixture density, defined as:

$$\rho_m = \sum_{k=1}^{n} \alpha_k \rho_k \tag{11}$$

In these expressions, α_k is the volume fraction of phase k, ρ_k is its density, $\overrightarrow{v_k}$ is its velocity vector, and n denotes the total number of phases.

The momentum conservation equation for the mixture is obtained by summing the individual momentum equations for each phase. It is expressed as follows:

$$\frac{\partial}{\partial t}(\rho_m \vec{v}_m) + \nabla \cdot (\rho_m \vec{v}_m \vec{v}_m) = -\nabla p + \nabla \cdot [\mu_m (\nabla \vec{v}_m + \nabla \vec{v}_m^T)] + \rho_m \vec{g} + \vec{F} - \nabla \cdot \left(\sum_{k=1}^{n} \alpha_k \rho_k \vec{v}_{dr,k} \vec{v}_{dr,k}\right) \quad (12)$$

Where p is the pressure shared by the phases, $\vec{g}$ is the acceleration due to gravity, and $\vec{F}$ represents external body forces (such as surface tension forces). The dynamic viscosity of the mixture, μ_m, is calculated by:

$$\mu_m = \sum_{k=1}^{n} \alpha_k \mu_k \quad (13)$$

The last term on the right-hand side of the momentum equation represents the effect of slip between the phases. It depends on the drift velocity of phase k, denoted as $\vec{v}_{d_r,k}$, which is related to the relative velocity (or slip velocity) of the secondary phase with respect to the primary phase.

Finally, the distribution of the secondary phase is determined by solving its dedicated volume fraction equation:

$$\frac{\partial}{\partial t}(\alpha_p \rho_p) + \nabla \cdot (\alpha_p \rho_p \vec{v}_m) = -\nabla \cdot (\alpha_p \rho_p \vec{v}_{dr,p}) + \dot{m}_{qp} - \dot{m}_{pq} \quad (14)$$

Where the first term on the right-hand side accounts for diffusion due to slip, while $\dot{m_{qp}}$ and $\dot{m_{pq}}$ describe the mass transfer rates between phase q and phase p (during a cavitation or phase change process).

For a two-phase fluid system consisting of a liquid phase (water) and a vapor phase (water vapor), the continuity equation for the mixture is expressed in the following simplified form:

$$\frac{\partial}{\partial t}(\rho_m) + \nabla \cdot (\rho_m \vec{v}_m) = 0 \quad (15)$$

Where the mixture velocity $\overrightarrow{v_m}$ is mass-weighted by the liquid (l) and vapor (v) phases:

$$\vec{v}_m = {\alpha_l \rho_l \vec{v}_l + \alpha_v \rho_v \vec{v}_v}/{\rho_m} \quad (16)$$

The mixture density ρ_m is defined by the law of mixtures as a function of the volume fractions:

$$\rho_m = \alpha_l \rho_l + \alpha_v \rho_v \quad (17)$$

Since the volumes of both phases occupy the entire computational domain, the geometric closure constraint requires that:

$$\alpha_l + \alpha_v = 1 \quad (18)$$

The momentum conservation equation for the water–vapor mixture is formulated as follows:

$$\frac{\partial}{\partial t}(\rho_m \vec{v}_m) + \nabla \cdot (\rho_m \vec{v}_m \vec{v}_m) = -\nabla p + \nabla \cdot [\mu_m (\nabla \vec{v}_m + \nabla \vec{v}_m^T)] + \rho_m \vec{g} + \vec{F} - \nabla \cdot \left(\alpha_l \rho_l \vec{v}_{dr,l} \vec{v}_{dr,l} + \alpha_v \rho_v \vec{v}_{dr,v} \vec{v}_{dr,v}\right) \quad (19)$$

Where p represents the shared pressure, $\vec{g}$ is the acceleration due to gravity, and $\vec{F}$ models the body forces (such as surface tension at the liquid–vapor interface). The dynamic viscosity of the mixture, μ_m, is calculated by:

$$\mu_m = \alpha_l \mu_k + \alpha_v \mu_v \quad (20)$$

The vectors $\vec{v}_{d_r,l}$ and $\vec{v}_{d_r,v}$ denote the drift velocities of the liquid and vapor phases, respectively.

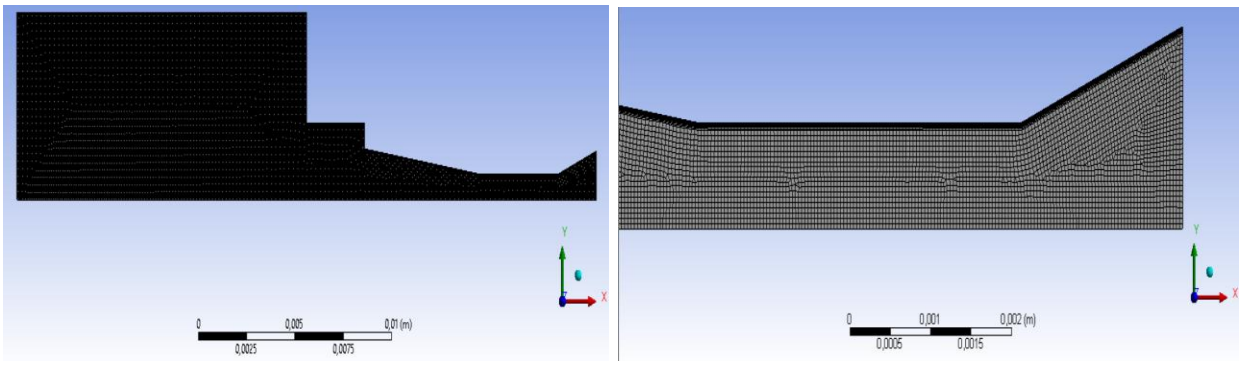
To track the dynamics of the cavitation process, the evolution of the dispersed phase (vapor) is governed by solving its dedicated volume fraction equation:

$$\frac{\partial}{\partial t}(\alpha_v \rho_v) + \nabla \cdot (\alpha_v \rho_v \vec{v}_m) = -\nabla \cdot \left(\alpha_v \rho_v \vec{v}_{dr,v}\right) + R_e - R_c \quad (21)$$

In this equation, the source terms on the right-hand side, R_e and R_c, represent the mass transfer rates related to evaporation (vapor generation due to cavitation) and condensation (vapor bubble implosion), respectively. These terms are calculated using the Zwart-Gerber-Belamri cavitation model.

2.3.3.2. Computational Domain and Boundary Conditions

The chosen viscosity model is the SST model within the K-ω framework. The K-ω SST (Shear Stress Transport) model accounts for the transport of the principal turbulent shear stress, which ensures its consistency with real turbulence at this scale and allows for a more accurate description of the spreading rate in circular jets. This model consists of two equations: the turbulent kinetic energy (k) equation and the specific dissipation rate (ω) equation.



(a) **(b)**

Figure 3. The numerical model of the cavitating nozzle ;(a) The complete model of the cavitating nozzle, (b) A close-up view of the cavitating nozzle throat.

Figure 3 presents the numerical model of a cavitating jet. The simulation domain is the internal flow field of the nozzle. Since the nozzle itself is an axisymmetric structure, a two-dimensional axisymmetric model was utilized to reduce computational time while ensuring simulation accuracy. The Mesh preprocessing software was used to generate the mesh for the model. A

pressure-inlet boundary condition was selected, and the total gauge pressure was set to 12 MPa ($1{,}2.10^7$). By utilizing Bernoulli's equation (Equation (22), the Reynolds number equation (Equation (22)), and the turbulence intensity calculation equation (Equation (23)), the inlet turbulence intensity was determined to be 5%.

$$p_g = p_s + \frac{1}{2}.\rho.u^2 \quad (22)$$

$$R_e = {\rho.u.l}/{\mu} \quad (23)$$

$$I = 0{,}16.R_e^{-0{,}125} \quad (24)$$

To accelerate convergence, the Coupled algorithm was used for the pressure-velocity coupling method. The spatial discretization adopted a second-order upwind scheme, a hybrid initialization was chosen, the number of iterations was set to 3000, and the residual convergence criterion was maintained at 10^{-5}.

2.3.3.3. Numerical Results and Discussion

- **Mesh Independence and Model Validation**

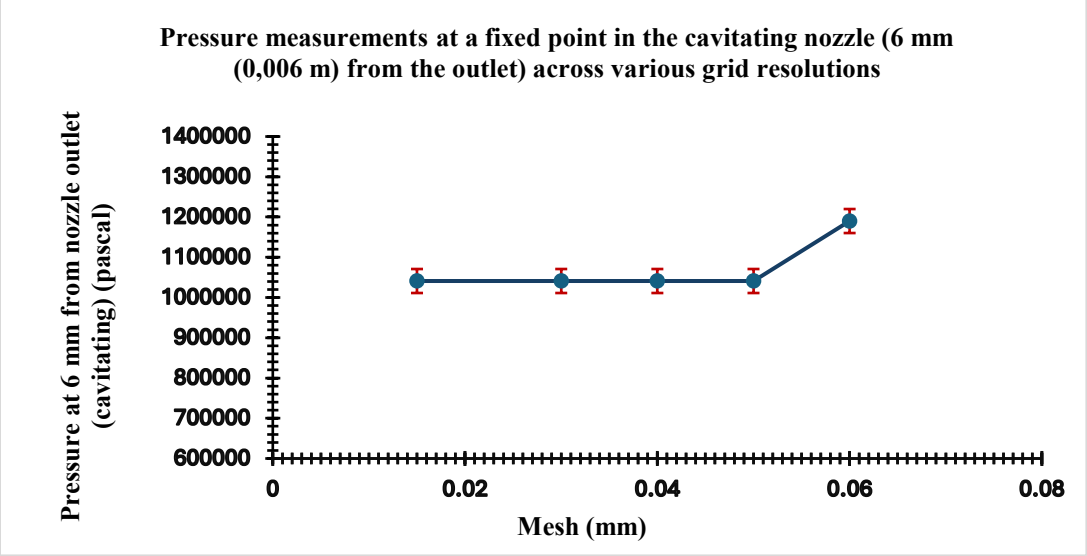


Figure 4. Pressure measurements at a fixed point in the cavitating nozzle (0,006 m from the outlet) across various grid resolutions.

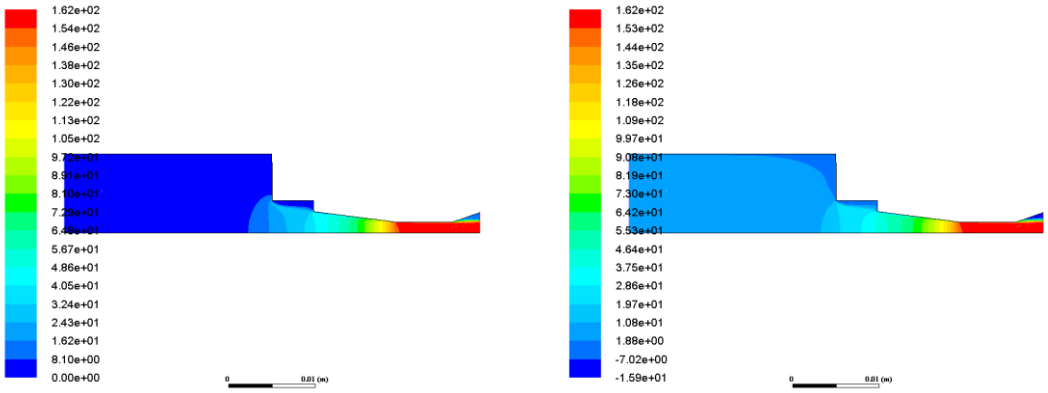
To ensure that the mesh quality does not affect the simulation results, a grid independence validation is required.

A grid independence study was conducted by evaluating the static pressure at a fixed location (0,006 m upstream of the nozzle outlet) across five different mesh sizes ranging from 0.0006 m to 0.00015 m (Figure 4). As shown in the figure, a clear numerical convergence is observed. For mesh sizes coarser than 0.00005 m (i.e., 0.0006 m), the pressure is significantly overpredicted due to the spatial resolution being insufficient to capture the steep pressure gradients and cavitation dynamics. However, from 0.0005 m down to 0.00015 m, the pressure stabilizes on a plateau at approximately 1.04 MPa ($1{,}04.10^7$ Pa), showing negligible variations that fall well within the numerical error bars. Therefore, the 0.0004 m mesh resolution was selected for all subsequent simulations, as it provides an optimal trade-off between physical accuracy and computational efficiency.

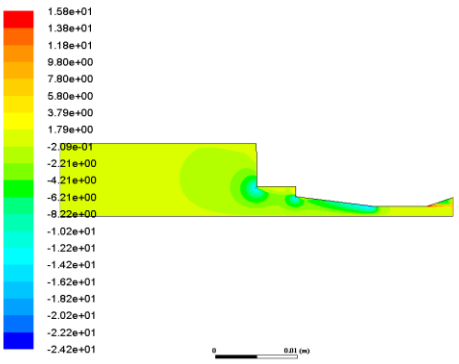
Furthermore, to ensure the validity of the near-wall mesh resolution and the turbulence model, the Wall y+ value was monitored along the nozzle walls. The area-weighted average y+ was found to be 1.64, with a maximum local value of 8.54. These values strictly satisfy the requirements of the near-wall modeling approach (such as the k-ω SST model), which typically demands a y+ close to 1 and strictly below 5 to 10 for enhanced wall treatment. This confirms that the boundary layer mesh is sufficiently refined to accurately capture the wall-bounded shear flows and separation dynamics inside the cavitating nozzle.

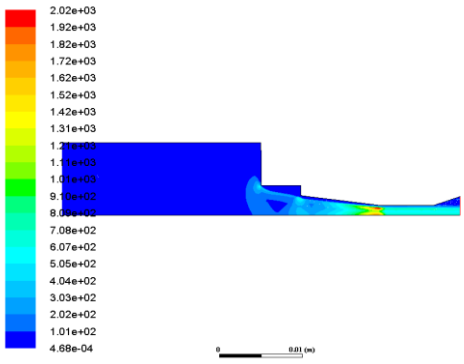
To ensure the physical validity and numerical robustness of the computational fluid dynamics (CFD) model, a rigorous monitoring of mass conservation was performed across the fluid domain. To overcome early numerical instabilities and suppress the mass flow oscillations encountered during steady-state resolutions, a transient formulation was adopted with a time step strictly adapted to the small geometric scale of 0,03 m**.** Upon completion of the calculation, the final mass balance extracted for the mixture yielded an inlet flow rate of 0.253415 kg/s and an outlet flow rate of -0.253450 kg/s, resulting in a residual net flux of only -3.52×10^{-5} kg/s. This corresponds to a relative mass conservation error of 0.014%, which is well below the standard 1% critical threshold commonly recommended in CFD literature. These statistics demonstrate excellent numerical convergence and confirm that the resolved hydrodynamic fields are highly reliable for subsequent physical analysis.

- **Flow Field Characteristics and Velocity Distribution**



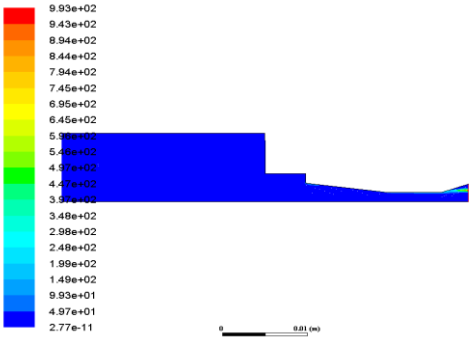
(a) (b)

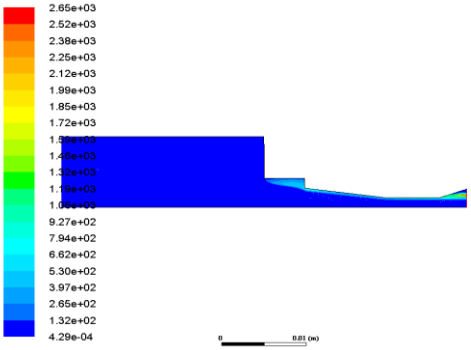




328

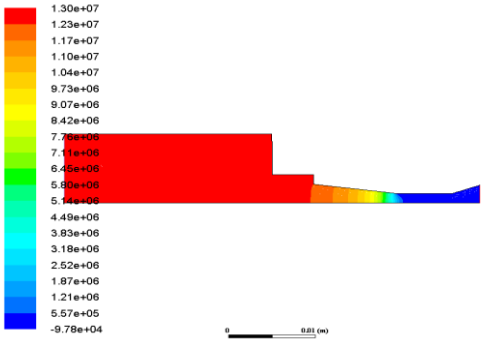
329 (c) (d)

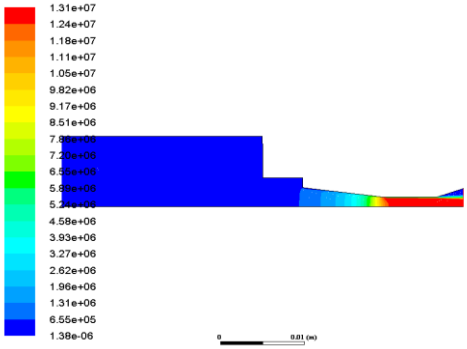




330

331 (e) (f)





332

333 (g) (h)

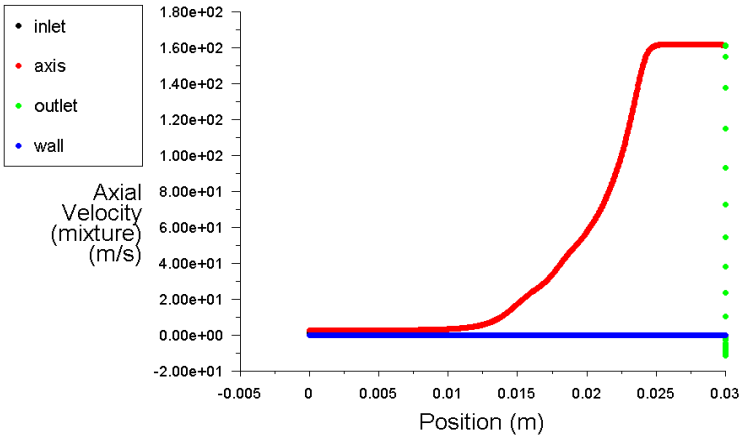
334 **Figure 5.** Numerical CFD contours of the flow characteristics and turbulence fields within the

335 cavitating nozzle: (a) velocity magnitude, (b) axial velocity, (c) radial velocity, (d) local Reynolds

number, (e) turbulent kinetic energy (k), and (f) turbulence intensity, (g) static pressure, (h) dynamic pressure.

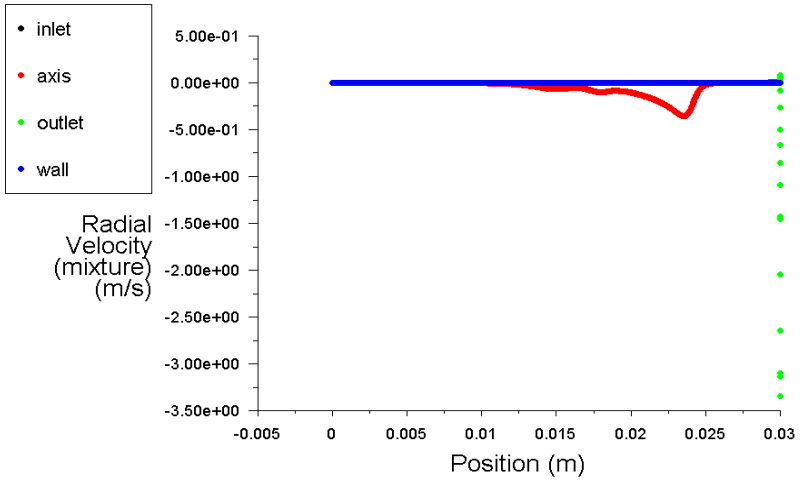
Figure 5 illustrates the numerical computational fluid dynamics (CFD) contours of the flow characteristics and turbulence fields within the cavitating nozzle, providing a comprehensive understanding of the global flow dynamics through the restriction. At the nozzle inlet, the flow initially exhibits a relatively low and uniform global and axial velocity (Figs. 5a, 5b), before undergoing a sudden and pronounced acceleration at the throat, where the axial velocity largely dominates the flow. Concurrently, the radial velocity variations (Fig. 5c) are concentrated near the sharp edge of the restriction, reflecting a vena contracta effect and a sudden change in the direction of the streamlines as the fluid bypasses the internal geometry of the nozzle. In accordance with Bernoulli's principle, this strong acceleration is accompanied by a sharp increase in dynamic pressure (Fig. 5h) and a drastic drop in static pressure (Fig. 5g), which reaches its minimum immediately downstream of the contraction; this local drop below the saturation vapor pressure confirms the thermodynamic triggering of cavitation in this region. Furthermore, the increase in the local Reynolds number downstream of the throat (Fig. 5d) indicates the maintenance of a highly turbulent regime, while the turbulent kinetic energy (Fig. 5e) and turbulence intensity (Fig. 5f) profiles reveal localized peaks along the shear layer, generated by the high velocity gradients between the high-speed core flow and the wall recirculation zones. These regions of high turbulence prove to be critical for the overall flow physics, as they accentuate turbulent pressure fluctuations, acting as a major driver for the onset and intensification of cavitation cloud shedding in this area. However, although these two-dimensional contour maps provide an excellent qualitative understanding of the flow structures, a refined, local characterization of the

359 hydrodynamic gradients remains indispensable. To accurately quantify these phenomena, the
360 evolution of quantitative velocity profiles (*XY* plots) along key cross-sectional and axial lines is
361 analyzed below, a quantitative study that is systematically correlated with the static pressure
362 distribution along the nozzle to mathematically link the local pressure drop to fluid acceleration
363 and the initiation of phase transition.



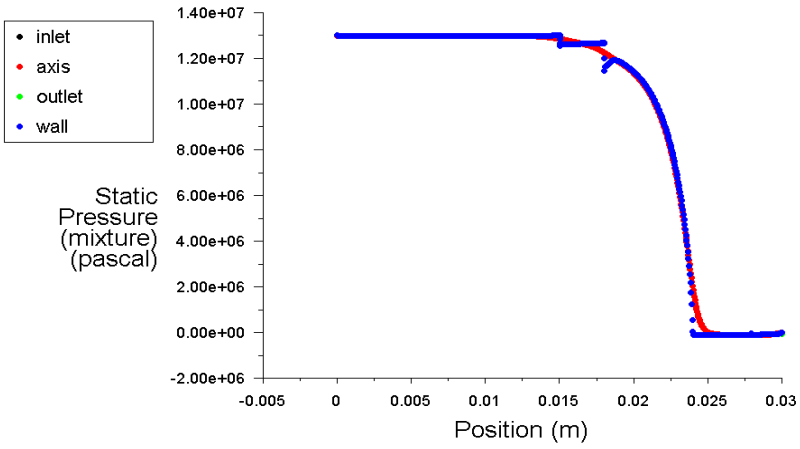
364

365 (a)



366

(b)



(c)

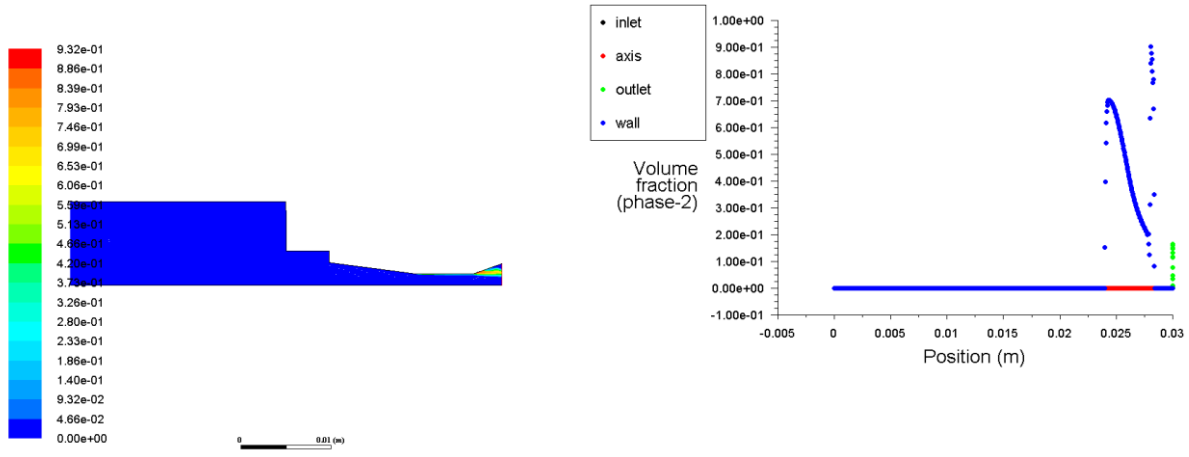
Figure 6. Quantitative XY profiles of the mixture flow characteristics along the nozzle centerline and boundaries: (a) axial velocity, (b) radial velocity, and (c) static pressure.

As depicted in Figure 6, the quantitative extraction of the hydrodynamic parameters confirms the strong coupling between the fluid acceleration and the local pressure drop. Specifically, the axial velocity profile (Fig. 6a) remains low and constant at approximately (10 m/s) in the inlet region (0 to 0.015 m). Beyond the position of (0.015 m), which marks the onset of the nozzle restriction, the axial velocity experiences a sharp, monotonic increase, reaching a maximum plateau of nearly (160 m/s) at (0.025 m) before exiting the nozzle. This rapid acceleration perfectly correlates with the dramatic collapse of the static pressure shown in Figure 6c. The static pressure drops abruptly from a high inlet pressure of (13 MPa) (1.3×10^7 Pa) down to near-zero values (close to the saturation vapor pressure) within the exact same spatial window (0.015 to 0.025 m), mathematically validating the Bernoulli effect and confirming that the geometric restriction forces

a massive conversion of pressure energy into kinetic energy. Concurrently, the radial velocity profile (Fig. 6b) exhibits a localized negative deflection (dipping down to approximately (-0.35 m/s) around the position of (0.023 m). This negative peak quantitatively substantiates the inward fluid redirection and the local flow contraction (vena contracta) near the restriction edge, highlighting the zone where the effective flow area is minimized and the turbulence initiation is most intense.

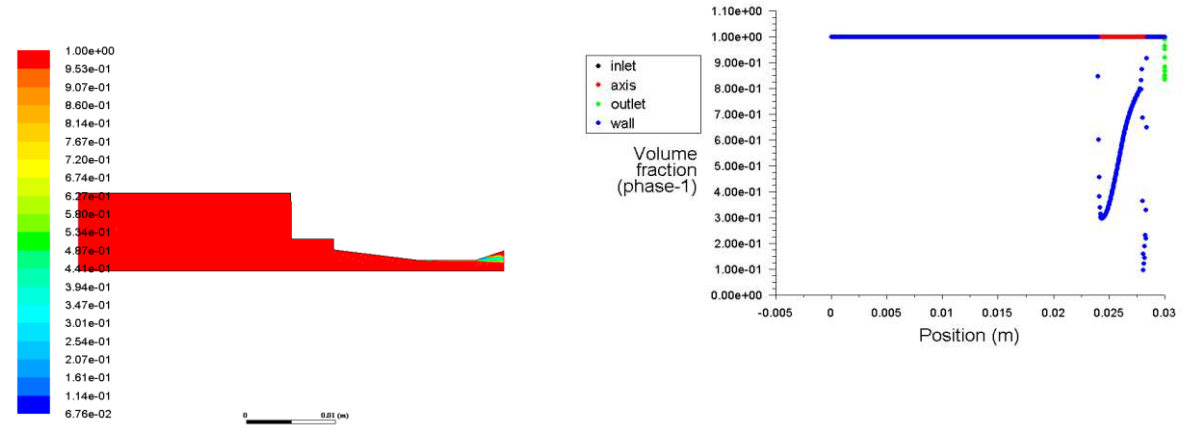
- **Cavitation Dynamics and Vapor Volume Fraction**

To visually and quantitatively complement the prior hydrodynamic analysis, Figure 6 illustrates the spatial distributions of the liquid and vapor phases, directly confirming the initiation of the phase transition. In the upstream region of the nozzle (0 to 0.023 m), the fluid remains entirely in the liquid phase, as indicated by a liquid volume fraction (phase-1) of 1.0 (Figs. 6c, 6d) and a vapor volume fraction (phase-2) of 0 (Figs. 7a, 7b). However, immediately downstream of the geometric restriction ($x > 0.023$ m), where the static pressure drops below the saturation vapor pressure, a sudden phase change occurs. The quantitative *XY* plot (Fig. 7b) shows a sharp increase in the vapor fraction, which peaks significantly along the nozzle walls and shear layers, reaching local values up to approximately 0.80 (80 % vapor content). This localized vaporization is mirrored by a concomitant drop in the liquid volume fraction (Fig. 7d), which plummets to a minimum of nearly 0.20 in the same core cavitating region. Near the nozzle outlet ($x = 0.03$ m), a progressive recovery is observed as the vapor fraction decreases and the liquid fraction returns toward unity, signifying a condensation zone. These results demonstrate that the geometric restriction acts as a strong trigger for hydrodynamic cavitation, successfully capturing the spatial expansion and subsequent collapse of the vapor cloud.



405

406 **(a)** **(b)**



407

408 **(c)** **(d)**

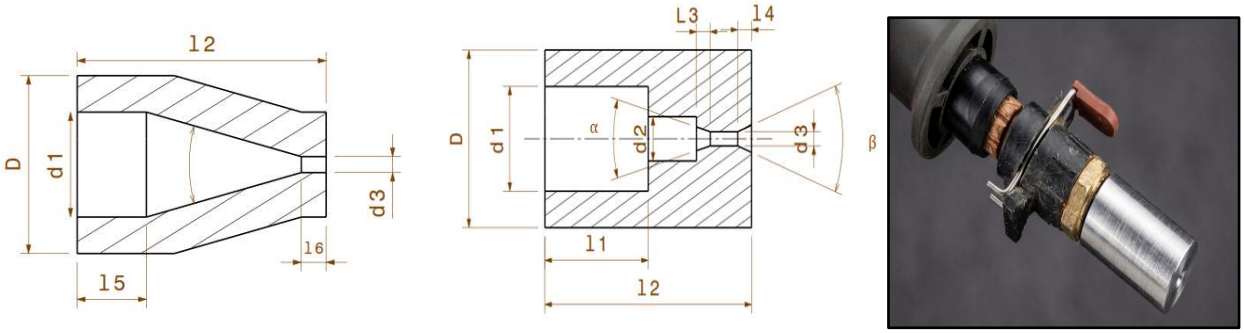
409 **Figure 7.** Qualitative *2D* contours and quantitative *XY* profiles of phase volume fractions within
410 the cavitating nozzle: (a) contours of vapor volume fraction (phase-2), (b) quantitative distribution
411 of phase-2, (c) contours of liquid volume fraction (phase-1), and (d) quantitative distribution of
412 phase-1.

413 In conclusion, the numerical CFD analysis successfully characterizes the complex hydrodynamic
414 behavior within the nozzle, mapping the critical zones of intense pressure drop, severe turbulence,
415 and high vapor phase fraction. While these computational findings provide essential insights into

the physical mechanisms driving the cavitation onset, they also pinpoint the exact regions subject to high mechanical stress and potential erosion. Consequently, managing these hydrodynamic phenomena is crucial not only for performance optimization but also for ensuring component durability. To bridge the gap between these theoretical fluid dynamics and practical application, the subsequent section shifts the focus toward the Fabrication and Cost analysis, evaluating the manufacturing feasibility, material selection, and economic viability of the proposed nozzle design.

2.3.4. Fabrication and cost

The nozzle was CNC-machined in-house from AISI 316 L bar stock, chosen for seawater corrosion resistance and machinability, with ±0.0005 m tolerances on all critical throat and divergent dimensions, verified by calibrated optical metrology (Figure 8). To better appreciate this design, compares the geometry of a conventional nozzle with that of our manufactured cavitating nozzle (Table 3). It operates over [8.10^6 – $2{,}5.10^7$] Pascal and connects to standard high-pressure pumps or pressure washers, avoiding proprietary equipment. The raw-material cost was below €40, whereas commercial cavitating nozzles of comparable specification ([1.10^7 -$2{,}5.10^7$] Pascal, throat [0,0015-0,002] m) are typically [3000-5000] €, and complete professional systems range from ~USD 3000 to over USD 55000. The design thus achieves a cost reduction exceeding 99% while preserving the geometric accuracy required for effective cavitation [39-22], removing the primary economic barrier to integrating cavitation-based cleaning into autonomous underwater maintenance systems.



(a) (b) (c)

Figure 8. Geometry comparison and nozzle prototype overview: (a) CAD schematic of the conventional nozzle, (b) CAD schematic of the cavitating nozzle, and (c) photograph of the fabricated AISI 316L stainless-steel nozzle used in the experimental campaign.

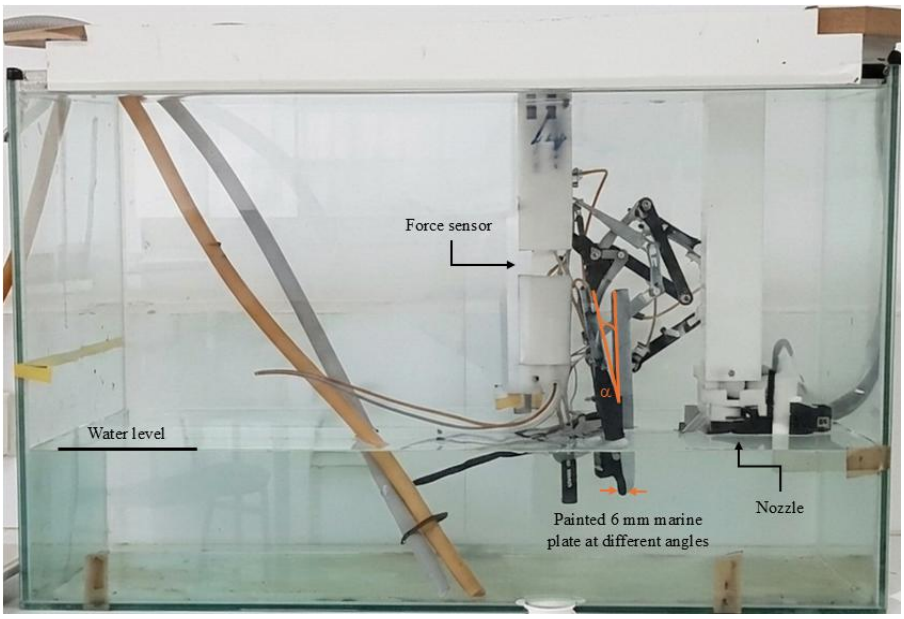
Table 3. Geometric parameters of the nozzle

Parameter	Value	Unit
D	0,02	m
d_1	0,0118	m
d_2	0,005	m
d_3	0,0016	m
l_1	0,015	m
l_2	0,03	m
l_3	0,002	m
l_4	0,002	m
l_5	0,008	m
l_6	0,003	m
α	0,524	rad
β	0,067	rad

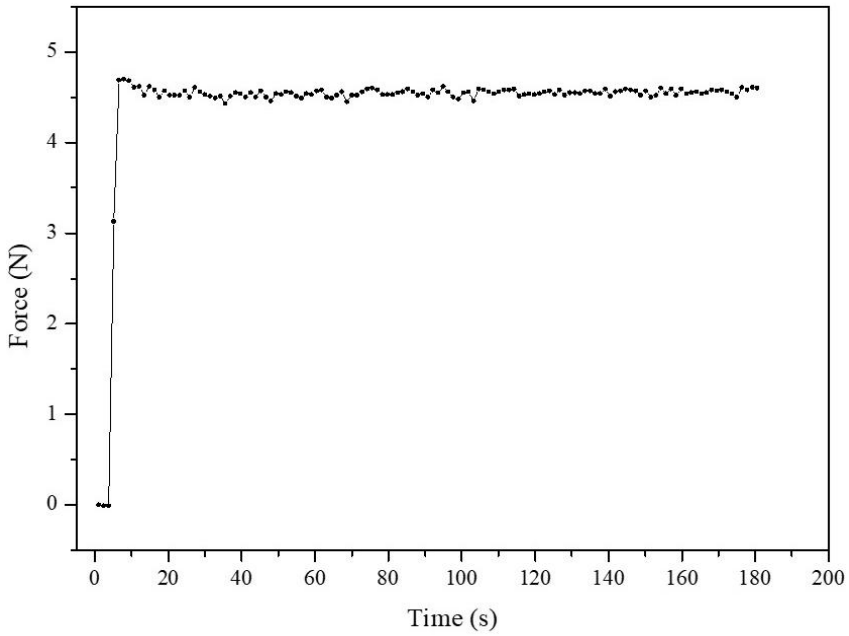
2.4. Experimental configuration

2.4.1. Test tank and hydraulic circuit

Tests were performed in a closed-loop facility (Figure 9). The test section was a rectangular tank (1,5 × 0,7 × 0,6 m, ≈ 0,63 m^3) with 0,01 m transparent polycarbonate walls for optical access, filled with fresh water at 20 ± 2 °C and stabilized for at least 30 min before each series. The interaction zone was kept 0,3 ± 0,01 m below the free surface for consistent back-pressure. The high-pressure circuit used a triplex plunger pump (8.10^6-$1{,}3.10^7$ pascal) feeding the nozzle through stainless-steel tubing; an inline turbine flow meter (±0.5% FS) confirmed $Q = 1{,}17 \times 10^{-4}$ m^3/s, and an upstream gauge ([0-2,5].10^7 Pascal, 1.10^5 Pascal resolution) recorded pressure. For conventional-jet tests, the Venturi nozzle was replaced by a plain circular orifice of equal throat diameter (0,0016 m) under identical hydraulic conditions.



(a)



(b)

Figure 9. Experimental configuration: (a) submerged cavitating-jet test bench with coated steel substrate; (b) representative temporal evolution of the normal impact force during jet-surface interaction.

2.4.2. Substrate positioning

The coated plate was mounted on a two-axis positioning system providing independent control of stand-off distance ([0,01-0,35] m, motorized linear stage, ±0.0005 m) and incidence angle θ (0,349 rad, 0,436 rad, 0,523 rad, 0,786 rad, 1,57 rad, rotary stage, ±0,01745 rad). The frame was anchored to the tank floor to suppress pump-borne vibration, and the nozzle axis was kept perpendicular to the positioning plane.

2.4.3. Force measurement and acquisition

Jet loading was measured with a single-axis strain-gauge load cell (10 N capacity, resolution < 0.01 N, 150% overload protection) mounted on the rear plate face via a rigid aluminum bracket

and enclosed in an IP68 housing [40]. The assembly natural frequency was estimated as $f_n = (1/2\pi)\sqrt{(k_{eff}/m_{eff})}$, with $k_{eff} \approx 8.2 \times 10^5$ N/m and $m_{eff} \approx 0.85$ kg, giving $f_n \approx 156$ Hz. Because the dominant cavitating-jet forcing frequencies lie below 80 Hz (FFT peak at 34 ± 6 Hz), the ratio $f_n/f_{forcing} > 1.9$, confirming dynamic fidelity without resonance amplification. Signals were conditioned (gain 500, CMRR > 100 dB) and sampled at 1 kHz with an Arduino Mega 2560 system, a platform validated against commercial acquisition hardware for fluid-mechanics measurements [41]. Data were processed in MATLAB R2023a with a 4th-order zero-phase Butterworth low-pass filter (f_c = 100 Hz) applied forward and backward to avoid phase distortion [42], the steady-state value was the mean over the central 60 s of each 120 s window after stationarity verification.

2.4.4. Optical diagnostics

Jet-surface interaction was recorded with a high-speed-capable camera at 240 fps (1/2000 s, 1080p) placed 0,4 m laterally, with tangential LED illumination. While 240 fps cannot resolve individual bubble collapse (~[1-100] µs ([1-100].10^{-6} s)), it adequately captures jet spreading, cavitation-cloud extent, and macroscopic fouling detachment [43], a 30 s sequence per condition was qualitatively analyzed against the force signal.

2.4.5. Reproducibility

Each condition was repeated n = 3 times with full system reset (tank restabilization, repositioning, calibration check). The coefficient of variation of the steady-state force was computed for all conditions; those with CV > 5% were repeated a fourth time. Results report means with standard deviations across repetitions.

The primary operational parameters and instrumentation specifications utilized during the experimental campaign are summarized in Table 4.

Table 4. Summary of experimental parameters and instrumentation.

Tank dimensions	1,5 × 0,7 × 0,6 m (≈ 0,63 m^3)
Working fluid	fresh water, 293,15 ± 2 K
Submersion depth	0,3 ± 0,01 m
Operating pressure	1,2.10^7 pascal (8.10^6-1,3.10^7 pascal range)
Flow rate	1,17.10^{-4} m^3/s (±0.5%)
Stand-off range	0,01-0,35 m (±0.0005 m)
Incidence angles	0,349 rad, 0,436 rad, 0,523 rad, 0,786 rad, 1,57 rad (±0,017 rad)
Load cell	10 N capacity, < 0.01 N resolution
Sampling frequency	1 kHz
Signal filter	4th-order Butterworth LP, f_c = 100 Hz
Acquisition per run	120 s (central 60 s averaged)
Repetitions	n = 3
Camera	240 fps, 1080p

2.5. Data analysis and uncertainty

The campaign was a full-factorial study of stand-off distance d (12 levels: 0,01, 0,02, 0,03, 0,04, 0,05, 0,075, 0,1, 0,15, 0,2, 0,25, 0,3, 0,35 m) and incidence angle θ (5 levels), for two jet types,

yielding 2 × 12 × 5 = 120 conditions, each repeated three times (360 runs). Pressure, flow rate, temperature, and depth were held constant. Raw signals were baseline-corrected, low-pass filtered (zero-phase), checked for stationarity (augmented Dickey-Fuller test, $\alpha = 0.05$), averaged over the central 60 s, and cleaned of $> 3\sigma$ outliers (< 2% of points per valid run).

The combined measurement uncertainty on the steady-state force was estimated following the GUM framework [44-45]. The dominant contributions (Table 5) give a combined standard uncertainty $u_c \approx 0.07$ N and an expanded uncertainty U = ± 0.14 N (k = 2, 95%) — about 3.1% of the nominal cavitating force (~4.5 N) and 1.2% of the nominal conventional force (~11 N). Reported error bars are the larger of the repetition standard deviation and U.

Table 5. Uncertainty budget for the steady-state force measurement (GUM framework).

Source	Type	Std. uncertainty	Contribution
Load-cell calibration	B	± 0.05 N	0.050 N
Load-cell resolution	B	± 0.005 N	0.005 N
Signal noise (post-filter)	A	run-specific	< 0.02 N
Temperature drift	B	± 0.01 N/k × 275,15 k	0.020 N
Positioning (stand-off)	B	± 0.0005 m	< 0.03 N
Angular alignment	B	±0,017 rad	< 0.02 N
Combined standard uncertainty	-	-	$u_c \approx 0.07$ N
Expanded uncertainty (k = 2)	-	-	U ≈ ± 0.14 N

Predictive capability was assessed by comparing the measured normal force with the theoretical value from Eq. (6) via the relative error δ (%) and the RMSE across stand-off distances at each angle. Cleaning performance was quantified before and after each test by ImageJ image analysis

(cleaning efficiency η), contact profilometry (Ra, Rz; ISO 4287), and dry-film-thickness monitoring (ISO 19840), a post-cleaning DFT loss exceeding 5 µm at any point defined the coating-damage threshold. Cleaning efficiency is defined as $\eta = (A_{fouled,before} - A_{fouled,after})/A_{fouled,before} \times 100$.

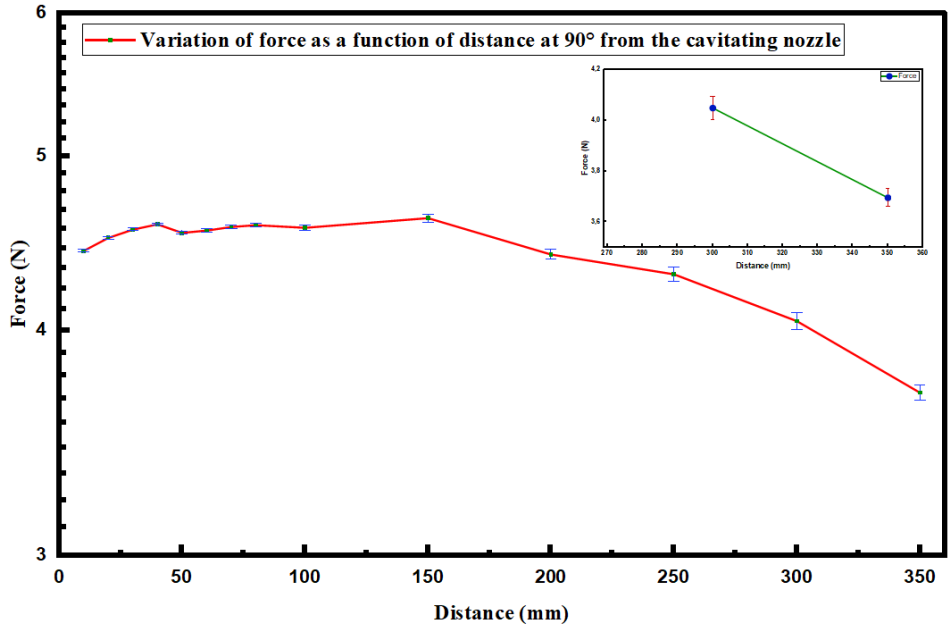
3. Results and Discussion

3.1. Effect of stand-off distance at normal incidence (θ = 1,57 rad)

Figure 10 shows the steady-state normal force F_n versus stand-off distance d at normal incidence for both jets, error bars combine $U = \pm$ 0.14 N with the repetition standard deviation. Over d = [0,01-0,04] m the cavitating jet produces a quasi-stable 4.5 ± 0.2 N, beyond 0,04 m it decreases monotonically to ≈ 3.5 ± 0.2 N at 0,35 m — only a 22% reduction across the full range. This force persistence is the defining operational advantage of cavitating jets.

The behaviour is consistent with the evolution of the local cavitation number. Using a free-jet centreline decay $V(d) = V_{th} \cdot d_{th}/(0.096\, d + d_{th})$, $\sigma(d) = (P_{out} - P_v)/(½\rho V(d)^2)$ rises with distance as the jet decelerates, so cavitation is most developed in the near field and weakens progressively downstream; the near-plateau force reflects the sustained collapse activity within the near-to-intermediate field, while the gradual decrease beyond ≈ 0,2 m marks the transition toward partial cavitation. This constitutes, to our knowledge, the first $\sigma(d)$ characterization under fully submerged marine-coating conditions.

The theoretical normal force at θ = 1,57 rad from Eq. (6) is $F_{n,theory} = \rho A[V^2(1 + C_c) + V_{rms}^2] =$ 3.40 × 1.27 + 0.18 = 4.50 N, matching the calibration point (d = 0,02 m) by construction. Across the plateau (d = 0,01-0,2 m) the model predicts the measured force within ± 8%, confirming that the calibrated three-component formulation captures the dominant physics in this regime.



528

529 **Figure 10.** Steady-state normal impact force F_n versus stand-off distance d at normal incidence
530 (θ = 1,57 rad) for the cavitating and conventional jets. Error bars combine the expanded
531 uncertainty (U = ± 0.14 N) and the standard deviation across n = 3 repetitions.

532 **3.2. Combined effect of stand-off distance and incidence angle**

533 Figure 11 shows F_n versus stand-off distance for oblique angles (θ = 0,349 rad, 0,436 rad, 0,524
534 rad, 0,785 rad) alongside θ = 1,57 rad. Two trends are consistent across angles: (i) F_n decreases
535 monotonically with distance, more steeply at lower angles owing to greater in-plane jet spreading;
536 and (ii) at any distance, F_n decreases with decreasing angle, following the sine projection of Eq.
537 (6), $F_n = F_{total}\ sin\ \theta$. At d = 0,02 m the measured forces are ≈ 4.5 N (1,57 rad), 4.0 N (0,785 rad),
538 3.2 N (0,524 rad), 2.8 N (0,436 rad), and 2.5 N (0,349 rad), agreeing with the sine law within ±
539 8% and confirming the angular-decomposition model. The near-grazing angle θ = 0,349 rad
540 maximizes the tangential component $F_t = F_{total}\ cos\ \theta$, favouring shear-driven removal of weakly
541 adherent biofilm and algal films [7]. The range θ = [0,524 -0,785] rad offers the best compromise

between normal (interfacial fatigue) and tangential (material transport) loading, in agreement with hydroblasting practice [7] and consistent with the cleaning-efficiency measurements of Section 3.4 — here extended to the cavitating-jet regime for the first time.

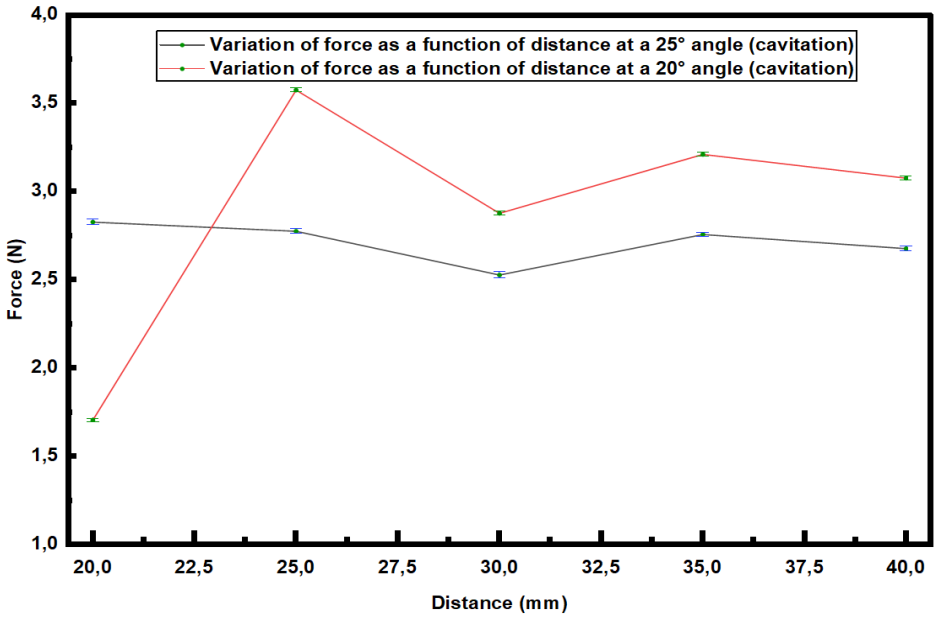


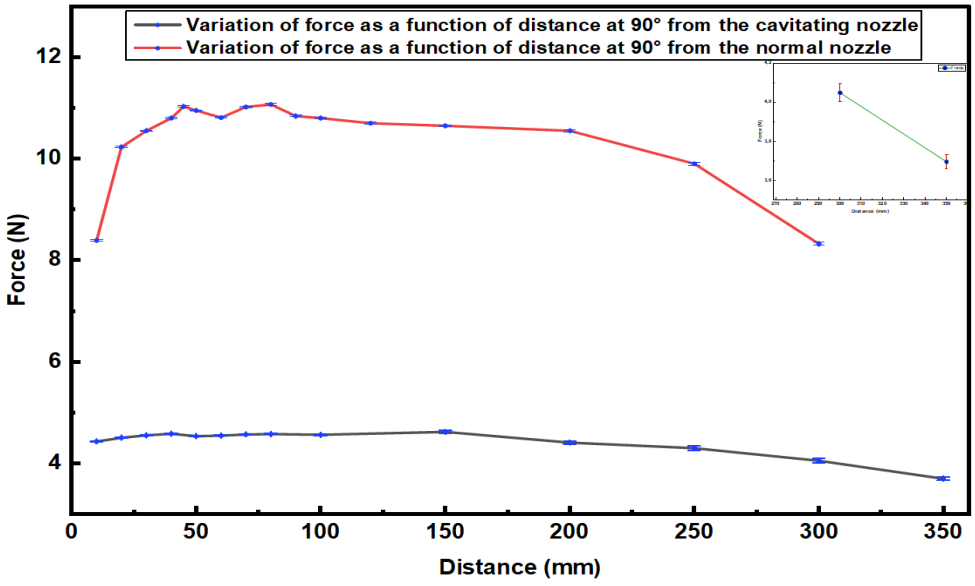
Figure 11. Normal impact force F_n versus stand-off distance for oblique incidence angles (θ = 0,349 rad, 0,436 rad, 0,524 rad, 0,785 rad) with the normal-incidence reference (θ = 1,57 rad).

3.3. Comparison between conventional and cavitating jets

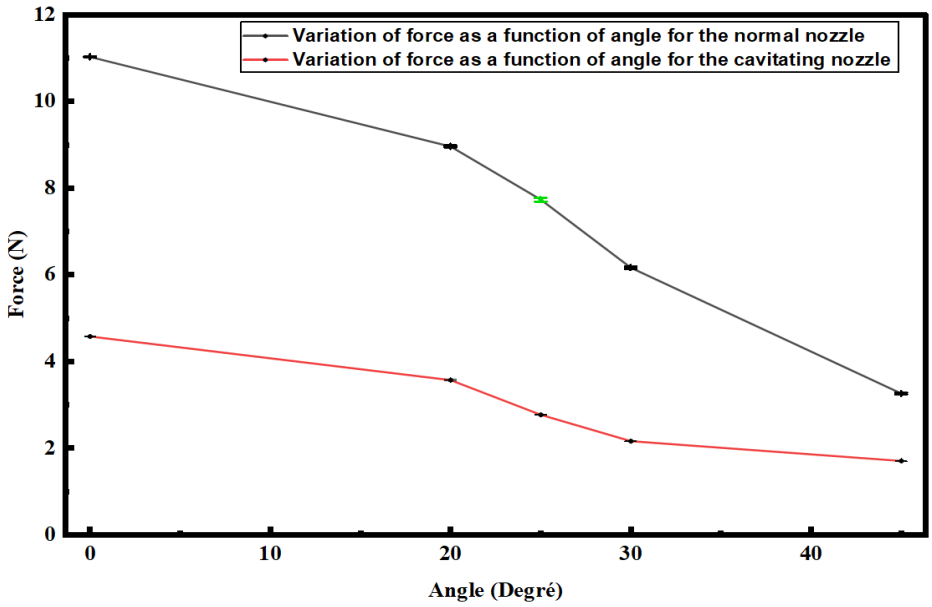
Figure 12 compares the two jets at θ = 1,57 rad (a) and across angles at d = 0,02 m (b) — the central comparison of the study. At normal incidence the conventional jet reaches a higher peak, ≈ 11.0 ± 0.2 N at short stand-off ($d \leq$ 0,02 m), but decays rapidly (well fitted by $F_{conv(d)} = 11.0 \exp(-0.004.d)$, $R^2 \approx 0.94$), retaining about 55% of its peak at 0,150 m and 30% at 0,3 m. The cavitating jet peaks lower (≈ 4.5 ± 0.2 N) but retains ~90% of its peak at 0,15 m and ~78% at 0,35 m. Consequently the two curves converge with distance: beyond $d \approx$ 0,29 m the cavitating force exceeds the conventional force within the tested range. The key distinction is therefore not peak

556 magnitude but force-to-distance persistence — directly relevant to robotic cleaning at variable
557 stand-off — consistent with the qualitative observations of Soyama and Yang [46], and reported
558 here for the first time under fully submerged marine-coating conditions.

559 Angular dependence (Figure 12b): the conventional jet loses about 75% of its normal-incidence
560 force at θ = 0,524 rad, whereas the cavitating jet retains about 55%. This superior angular
561 robustness follows from the distributed nature of cavitation-collapse events, which are not
562 geometrically confined to the jet axis and remain partially effective across a wider range of
563 impingement configurations — valuable for cleaning curved hulls with variable local incidence
564 [39]. From a coating-protection standpoint, the high conventional peak (~11 N) concentrated over
565 a very small area at short stand-off generates a stress concentration exceeding common antifouling-
566 topcoat adhesion, producing the damage documented in Section 3.4, the spatially distributed,
567 temporally stable cavitating-jet profile remained below the damage threshold across all tested
568 conditions [47].



(a)



(b)

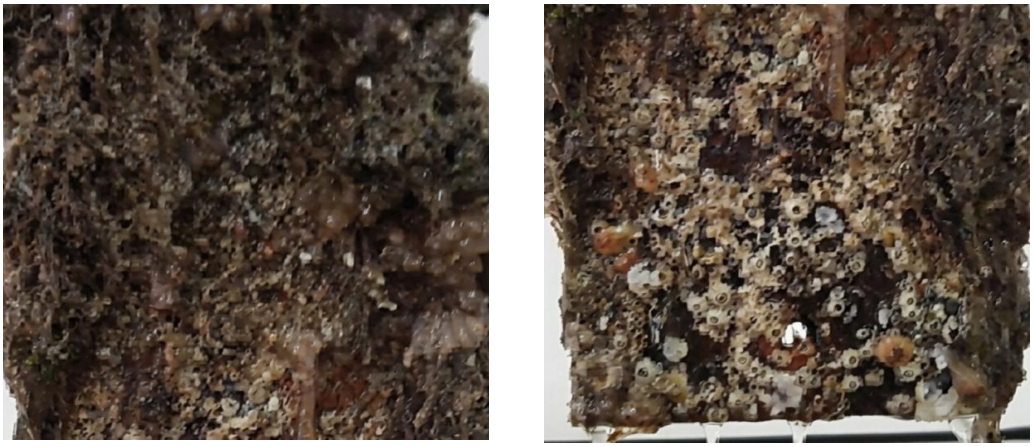
569 **Figure 12.** Comparison of conventional and cavitating jets: (a) normal force versus stand-off
570 distance at θ = 1,57 rad; (b) normal force versus incidence angle at d = 0,02 m.

571 **3.4. Cleaning performance and coating integrity**

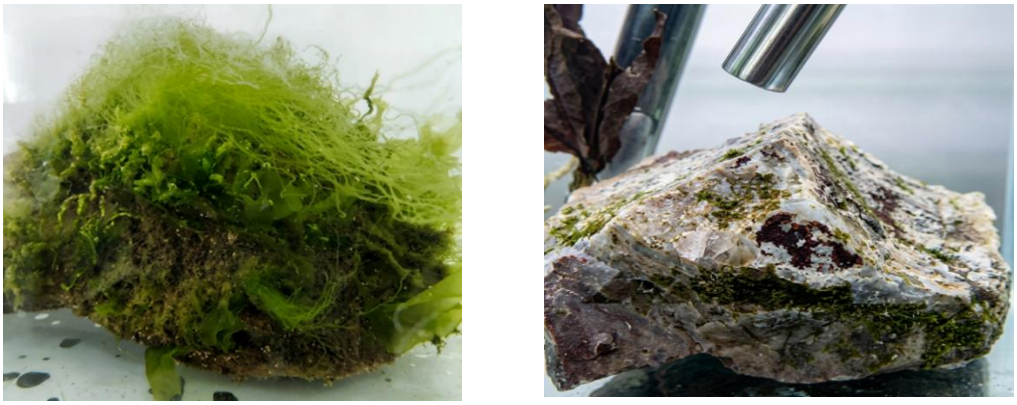
572 Figure 13 presents before/after characterization at the optimal cavitating condition (d = [0,02-0,04]
573 m, θ = [0,524 - 0,785] rad, 1,2.10^7 Pascal, 120 s). ImageJ analysis (n = 6 pairs) gave a mean
574 cleaning efficiency η = 72 ± 6% for the cavitating jet, versus η = 88 ± 4% for the conventional jet
575 at its optimal short-distance condition (d = [0,004-0,006] m, θ = 1,57 rad), both removed
576 macrofouling effectively, the lower cavitating value reflecting incomplete removal of basal
577 barnacle-adhesive residue. Post-cleaning profilometry (ISO 4287, n = 5) showed ΔRa = 0.18 ±
578 0.08 µm (0.18 ± 0.08 .10^{-6} m) for the cavitating jet (Ra_{after} = 28.6 µm, statistically non-significant,
579 paired t-test p = 0.23), versus ΔRa = 2.4 ± 0.6 µm (2.4 ± 0.6 .10^{-6} m) for the conventional jet at d
580 < 0,01 m (exceeding the 1.5 µm incipient-erosion threshold). Dry-film-thickness monitoring (ISO

19840) recorded no loss above the 5 µm damage threshold for any cavitating specimen within the optimal window (mean $\Delta DFT = -1.2 \pm 0.8$ µm ($-1.2 \pm 0.8 .10^{-6}$ m), within the ±1 µm ($\pm 1. 10^{-6}$ m) gauge uncertainty), whereas conventional cleaning at $d < 0{,}01$ m gave a mean DFT loss of 8.4 ± 1.9 µm ($8.4 \pm 1.9 .10^{-6}$ m) ($p < 0.01$), consistent with topcoat erosion under repeated high-frequency impact [Cao Y.P. et al., 2022, Momber A.W., 2024]. These results confirm that the cavitating jet removes biofouling effectively while fully preserving coating integrity within the identified window, validating the primary hypothesis.

Before **After**



(a)



(b)

588 **Figure 13.** Cavitating-jet cleaning performance: (a) before/after view of a coated steel plate
589 showing effective fouling removal without coating degradation (tangential illumination), (b)
590 comparative fouling removal by the cavitating and conventional jets under identical operating
591 conditions.

592 **3.5. Physical mechanisms, operational implications, and limitations**

593 Physical mechanisms. The force stability of the cavitating jet over extended distances arises from
594 the interplay between primary jet-momentum decay and secondary bubble-collapse energy. As σ
595 increases with distance, the spatial distribution of collapse events shifts and the peak erosive action
596 moves toward intermediate distances, a mechanism described by Franc & Michel and here
597 confirmed quantitatively under submerged marine-coating conditions.

598 Operational implications. The optimal window (d = [0,02-0,04] m, θ = [0,524 - 0,785] rad)
599 translates directly into stand-off-control specifications for autonomous cleaning robots. The
600 cavitating-jet force stability provides a ±0,01 m tolerance around the target distance, relaxing the
601 positioning precision required of the robotic platform relative to conventional jets (< ±0,002 m).
602 Combined with the sub-€40 nozzle, this establishes a technically and economically viable path to
603 wide-scale deployment.

604 Comparison with the literature. The measured cavitating peak of 4.5 N at d = 0,02 m falls within
605 the 3-6 N range reported by Li & Soyama [Li D. and Soyama H., 2010] for comparable Venturi
606 nozzles at similar pressures, providing external validation, and the optimal [0,02-0,04] m window
607 overlaps the [0,03-0,05] m range identified by Zhong et al. for shear-type nozzles, indicating
608 generality across cavitation configurations.

Limitations. Three limitations should be noted. First, tests used static fresh water, whereas real operations involve seawater flow, ship motion, and varying hydrostatic pressure, which affect both the cavitation number and the effective stand-off. Second, the biofouling specimens, though grown under representative colonization conditions, were static-laboratory-cultured and may not fully reproduce mature oceanic biofilm mechanics. Third, the analytical model (Eqs. 6-7) neglects jet-surface confinement and the unsteady pressure field from bubble-cloud oscillations, so it captures the plateau within ±8% but is not expected to reproduce far-field cavitation-cloud dynamics; future work should combine field trials under dynamic conditions with coupled CFD-cavitation modelling of the jet-surface interaction.

4. Conclusion

This study quantified the hydrodynamic impact and cleaning performance of cavitating water jets on marine-coated steel, with direct comparison to conventional high-pressure jets, through the evolution of the normal impact force with stand-off distance and incidence angle under controlled submerged conditions. The cavitating jet exhibited a markedly more stable mechanical response over extended distances (only 22% force reduction over [0,01-0,35] m) than the conventional jet, which delivered a higher peak (~11 N) but decayed rapidly. Optimal cleaning was achieved at d = [0,02-0,04] m and θ = [0,524 - 0,785] rad, providing sufficient mechanical action without coating degradation, as confirmed by non-significant roughness change (ΔRa = +0,18 µm (0,18.10^{-6} m)) and no measurable film-thickness loss (ΔDFT = −1,2 µm (-1,2.10^{-6} m)), versus clear damage under short-distance conventional jetting. A calibrated three-component impact-force model (Cc = 0.27, $Vrms$ = 9.5 m/s) reproduced the measured plateau within ±8%.

In addition, computational fluid dynamics (CFD) simulations validated our nozzle design model, successfully confirming the onset and development of the underwater cavitation phenomenon. This coupled approach demonstrates the process's efficiency in removing biofouling under submerged conditions while preserving the hull's paint integrity. On an industrial scale, this technology offers major prospects for ecological transition and operational efficiency, significantly reducing ship maintenance costs, minimizing cleaning downtime, and optimizing fuel consumption through a perfectly cleaned hull.

Finally, an in-house Venturi cavitating nozzle was designed and validated at a material cost below €40 — a >99% reduction versus commercial equivalents — compatible with standard pumping equipment and suitable for integration into autonomous underwater cleaning robots. Future work should couple force measurement with detailed damage characterization and cavitation-intensity mapping to further optimize efficiency while ensuring long-term coating integrity.

Data availability

The datasets generated during this study — time-resolved force signals, surface-profilometry measurements, ImageJ fouling-coverage analyses, and dry-film-thickness records, and CFD simulation mesh and result files — are available from the corresponding author on reasonable request.

Disclosure

This work is part of the project “Underwater Surveillance Vehicle, Ship-Hull Inspector and Cleaner (PRAD A5P2), carried out at Laboratory LR-19-DN02, Tunisian Naval Academy, Menzel Bourguiba, Tunisia.

652 **Conflicts of interest**

653 The authors declare no conflict of interest.

654 **Author contributions**

655 A. Mouhli performed the experimental work and theoretical calculations. A. Mouhli and S.
656 Hachicha carried out the mechanical design of the nozzle, fabrication, and analysis of results.
657 Writing and revision were performed by A. Toumi and C. Mejri. The work was supervised by C.
658 Zaoui and A. Siala.

659 **Funding**

660 This work was funded by the Military Research Center (CRM) of Tunisia.

661 **Acknowledgments**

662 The authors gratefully acknowledge the Military Research Center of Tunisia (CRM) for the
663 opportunity to carry out this project.

664

References;

1. Schultz, M.P. “Effects of coating roughness and biofouling on ship resistance and powering. *Biofouling* 2007, **23**, 331-341.
2. Townsin, R.L., The ship hull fouling penalty. *Biofouling* 2003, **19** (Suppl.), 9-15.
3. Demirel, Y.K. et al., Predicting the effect of biofouling on ship resistance using CFD. *Appl. Ocean Res*. 2017, **62**, 100-118.
4. Schultz, M.P. et al., Economic impact of biofouling on a naval surface ship. *Biofouling* 2011, **27**, 87-98.
5. GloFouling Partnerships. London, Report (2021). Preliminary results: Impact of ships' biofouling on greenhouse gas emissions. International Maritime Organization (IMO). Disponible sur : Remove slime from ships to cut emissions
6. Liu, S. et al. The detrimental impact of biofilm on ship fuel consumption and CO2 emissions. *Ocean Eng*. 2025, **320**, 120-210.
7. Amara, I. Et al.. (2018). Antifouling processes and toxicity, *A review. Environmental Science and Pollution Research*, **25**, 25211–25226.
8. Zhu, H. et al.. “Cavitation-induced cleaning characteristics of barnacle fouling on hull surfaces using high-speed water jets.” *Ocean Engineering*, Volume **340**, Part 3 (2025).
9. Song, S. and Avan, I., Review of Underwater Ship Hull Cleaning Technologies, *Journal of Marine Science and Application*, vol. **19**, no. 3, pp. 415–429, Sep. 2020.

10. Maduka, M. et al.. “Hydrodynamic effects of biofouling-induced surface roughness – Review and research gaps for shallow water offshore wind energy structures.” *Ocean Engineering*, Volume **272** (2023).

11. Cao, Y.P. et al., Experimental study on surface erosion of Grade-A marine steel by ultrahigh-pressure water jet. *Water* 2022, **14**, 1953.

12. Zhang, Q.B. et al. Experimental study on the optimization of rust-removal effect on the surface of Grade-A marine steel by ultra-high-pressure water jet. *Metals* 2024, **14**, 1335.

13. Tribou, M. and Swain, G., Ship-hull in-water cleaning and its effects on fouling-control coatings. *Biofouling* 2020, **36**, 1-12.

14. . Yuan, T.P. et al.. “Aquaculture net cleaning with cavitation improves biofouling removal. “*Ocean Engineering*, Volume **285**, Part 1 (2023).

15. Stap, B. et al. Quantification of paint flakes and metal emissions during pro-active in-water hull cleaning. *Chemosphere* 2025, **370**, 143900.

16. Swain, G. Et al.. (2022). The transition from reactive cleaning to proactive grooming of ship hulls. *Marine Technology Society Journal*, **56**(2), 54–67.

17. Zhang, X.et al.. “Experimental and numerical investigation of cleaning performance of obliquely impinging cavitating jets for barnacle removal from hull surfaces” *Ocean Engineering*, Volume **365**, Part 4 (2026).

18. Brennen, C.E., 2013. A Review of the Dynamics of Cavitating Pumps. *Journal of Fluids Engineering*, Volume **135**, Numéro 6, Article 061301.

19. Soyama, H., Cavitation peening, a review. *J. Mater. Process. Technol*. 2015, **211**, 475-486.

706 20. Arndt, R.E.A., Cavitation in fluid machinery and hydraulic structures. Annu. *Rev. Fluid Mech*.
707 2002, **34**, 143-175.
708 21. Yang, Y. et al. Impact force of a cavitating jet versus stand-off distance: a high-speed imaging
709 study. *Shock Vib*. 2020, **2020**, 8813377.
710 22. Huang, S. Et al., "Research on Erosion Effect of Various Submerged Cavitating Jet Nozzles
711 and Design of Self-Rotating Cleaning Device, *Applied Sciences*, vol. 14, no. 4, p. **1433**, Feb.
712 2024.
713 23. Puc, U. Et al., Development and field testing of a cavitation-based robotic platform for
714 sustainable in-water hull cleaning. *J. Mar. Sci. Eng*. 2026, 14, **227**.
715 24. Fang, Z. et al. Cavitation-damage characteristics following marine-fouling cleaning by a self-
716 excited oscillation cavitation jet. *Appl. Ocean Res*. 2023, **138**, 103628.
717 25. ISO 8501-1, 2007. Preparation of Steel Substrates before Application of Paints and Related
718 Products, ISO: Geneva, Switzerland, 2007. ISO 8501-1:2007 Rust grades and preparation
719 grades of uncoated steel substrates and of steel substrates after overall removal of previous
720 coatings | Building CodeHub.
721 26. ISO 19840, 2012. Paints and Varnishes - Measurement of and Acceptance Criteria for the
722 Thickness of Dry Films on Rough Surfaces ISO: Geneva, Switzerland, 2012. ISO 19840:2012
723 - Paints and varnishes — Corrosion protection of steel structures by protective paint systems
724 — Measurement of, and acceptance criteria for, the thickness of dry films on rough surfaces.
725 27. Railkin, A.I., Marine Biofouling, Colonization Processes and Defenses CRC Press, Boca
726 Raton, FL, USA, 2004. https://doi.org/10.1201/9780203503232.

28. Dafforn, K.A. et al., Antifouling strategies: history and regulation, ecological impacts and mitigation. *Mar. Pollut. Bull*. 2011, **62**, 453-465.

29. ISO 4287, 1997. Geometrical Product Specifications - Surface Texture: Profile Method ISO: Geneva, Switzerland, 1997.

30. Salta, M. et al., Designing biomimetic antifouling surfaces. *Philos. Trans. R. Soc*. A 2013, **371**, 20120139.

31. Quinn, R.J., Experimental investigation of impinging turbulent water jets. *J. Fluids Eng.* (ASME) 1995, **117**, 673-679.

32. Franc, J.P. and Michel, J.M., Fundamentals of Cavitation Springer: Dordrecht, The Netherlands, 2005. https://doi.org/10.1007/1-4020-2233-6.

33. Li, D. and Soyama, H., Characteristics of a cavitating jet and its impact force. *J. Fluids Eng*. (ASME) 2010, **132**, 111303.

34. Ashrafizadeh, S.M. and Ghassemi, H., Experimental and numerical investigation on the performance of small-sized cavitating venturis. *Appl. Math. Model*. 2015, **39**, 1656-1666.

35. Saharan, V.K. et al. Optimization of Venturi-cavitator geometry for energy efficiency. *J. Hydrodyn*. 2016, **28**, 293-305.

36. Gaikwad, V. Et al.. (2025). Optimisation of tandem Venturi cavitation reactors. *Chemical Engineering and Processing - Process Intensification*, **207**, Article 110098.

37. Lieber, C.et al.. (2020). Spray evaporation of urea–water solution: Experiments and modelling. *Experimental Thermal and Fluid Science*, **116**, Article 110108.

38. Wang, Y. et al.. (2024). Floating-state calculation method based on tetrahedral meshing. *Ocean Engineering*, **297**, Article 117006.

749 39. Sahin, O. et al., Design and shape optimization of a strain-gauge load cell. *Sensors* 2022, **22**,
750 7508.

751 40. Dehghan Manshadi, M. et al., Design and development of a 5-channel Arduino-based data-
752 acquisition system for experimental aerodynamics research. *Sensors* 2018, **18**, 2382.

753 41. Li, X. et al., A robust zero-phase digital-filtering method for real-time signal-processing
754 applications. *J. Signal Process. Syst*. 2022, **94**, 785-796.

755 42. El Hassan, M. et al., A review of the erosion mechanism in cavitating jets and their industrial
756 applications. *Appl. Sci*. 2021, **11**, 3166.

757 43. ISO/IEC Guide 98-3, 2008. Uncertainty of Measurement - Part 3: Guide to the Expression of
758 Uncertainty in Measurement (GUM) ISO: Geneva, Switzerland, 2008. Disponible sur : ISO
759 Standard 50461 (Boutique de l'ISO - Norme 50461)(Consulté le 8 octobre 2026).

760 *44.* Possolo, A. and Toman, B., How accurate are your experimental data Int. *J. Thermophys.*
761 *2024, **45**, 12.*

762 45. Soyama, H., Cavitating jet, a review. *Appl. Sci*. 2020, **10**, 7280.

763 46. Schlichting, H. and Gersten, K. (2017). Boundary-Layer Theory (9e éd.). Springer Berlin
764 Heidelberg. https://doi.org/10.1007/978-3-662-52919-5.

765 47. Momber, A.W. et al., Effects of impact damage on the performance of offshore wind-power
766 coatings after accelerated ageing. *Corros. Eng. Sci. Technol*. 2024, **59**, 311-320.

Supplementary Files

This is a list of supplementary files associated with this preprint. Click to download.

- Tables.docx